Strain-based condition monitoring of inner raceways of deep-groove ball bearings using FBG sensors

Fernando de la Hucha Arce[1], Damilare Samuel Ojo[2], Abhinit Hirde[3],
Ted Ooijevaar[4], Francis Berghmans[5] and Sidney Goossens[6]

[1, 3, 4] *MotionS, Flanders Make, Gaston Geenslaan 8, 3001 Leuven, Belgium*
{*fernando.delahuchaarce, abhinit.hirde, ted.ooijevaar*}@*flandersmake.be*

[2, 5, 6] *Brussels Photonics (B-PHOT), Vrije Universiteit Brussel, Brussels, Belgium*
[2, 5, 6]*BP&M, Flanders Make@VUB, Brussels, Belgium*
{*damilare.samuel.ojo, francis.berghmans, sidney.goossens*}@*vub.be*

ABSTRACT

Rolling element bearings are critical components of rotating machinery, whose failure is one of the main causes of downtime and maintenance. Traditional methods of condition monitoring of bearings, based on accelerometers or acoustic emission sensors and vibration analysis, are prone to signal attenuation and interference in the transfer path due to other machine components. As an alternative, fiber Bragg grating (FBG) sensors allow for quasi-distributed sensing of the local strain of the bearing, as they can be integrated in a single optical fiber bonded directly onto a bearing raceway. They offer several advantages, such as compactness, immunity to electromagnetic interference (EMI), and resistance to corrosion. Proximity and the quasi-distributed nature of FBG-based strain sensing are key properties to obtain significantly higher signal-to-noise ratio (SNR) and sensitivity, enabling enhanced fault diagnosis and localization. In this work, we analyze the strain signals obtained during an accelerated lifetime test (ALT) of a deep-groove ball bearing. The FBGs are instrumented on the rotating inner raceway of the bearing, going beyond the implementation on the static outer raceway performed by several recent research works. We study the behaviour of the FBG signals and their features during the complete evolution of a surface-initiated fatigue fault on the inner ring, and evaluate their capabilities for simultaneous fault detection and localization. We observe that two features are reliable indicators for fault detection and localization, the RMS of the high-pass filtered FBG signals, and the sum of values of their squared envelope spectrum (SES) at the harmonics of the ball pass frequency on the inner race (BPFI), while the peak-to-peak (P2P) value is not.

1. INTRODUCTION

Rolling element bearings are crucial components of rotating machines employed in several important industrial sectors, including manufacturing, aerospace, energy, and transportation. Bearing failure can cause severe machine damage and even complete breakdown, making it a significant source of downtime and maintenance costs. To reduce both, condition-based maintenance strategies aim to schedule maintenance actions based on the current health diagnosis of machine components (Jardine, Lin, & Banjevic, 2006; Quatrini, Costantino, Di Gravio, & Patriarca, 2020). A critical step to enable these strategies is condition monitoring of bearings, in particular early and reliable fault detection.

Traditional bearing diagnosis is a well-established field, relying on different sensor technologies such as accelerometers (Randall & Antoni, 2011), microphones (Eryilmaz, de la Hucha Arce, Zegers, & Ooijevaar, 2024), and acoustic emission sensors (Zhang, Borghesani, Randall, & Peng, 2022). Nevertheless, they present certain inherent limitations. First, the sensors must often be mounted away from the fault location, which introduces signal attenuation and transfer path effects that must be compensated (Randall, 2011). Second, typically only a few sensors can be feasibly installed, especially in complicated machine structures, which limits scalability and the ability to localize a fault. Finally, the indirect nature of these measurements creates difficulties to robustly estimate the severity of a fault (Zhang et al., 2022).

To attempt to overcome these limitations, research is being conducted on optical fiber Bragg grating (FBG) sensors as an alternative technology for diagnosis of rotating machinery (Medvedovsky, Ohana, Klein, Tur, & Bortman, 2022; Brusamarello, Cardozo da Silva, de Morais Sousa, & Guarneri, 2023). Due to their small dimensions, FBG sensors can be installed in close proximity of the bearing (Medvedovsky et al.,

---

2022), and even directly on the bearing's rings (Goossens et al., 2025). This offers the possibility of higher signal-to-noise ratio (SNR) and sensitivity to the local strain evolution associated with fault development. Multiple FBGs can be integrated in a single optical fiber and, since they support multiplexing (Goossens et al., 2021), enable quasi-distributed sensing of the local strain of the bearing. Moreover, they are immune to electromagnetic interference (EMI) and resistant to corrosion, which are advantageous properties in certain environments where electrical sensors would create safety risks.

In this work, we analyze the fault detection and localization capabilities of a quasi-distributed sensing network of FBGs instrumented on the bearing's inner ring over the course of an accelerated lifetime test. In this experiment, a deep-groove ball bearing runs to its end-of-life while a surface-initiated fatigue fault evolves from an initial micro-indentation to a fully developed spall. The sensing system consists of nineteen (19) FBGs integrated on a single fiber, bonded directly to the rotating inner ring by the adhesive-based technique demonstrated in (Goossens et al., 2025). To the best of our knowledge, this is the first accelerated lifetime study of a bearing with FBGs instrumented directly on its inner ring. We characterize the acquired FBG signals and, based on this analysis, study the behaviour of some of their features over the course of the fault development, evaluating their capabilities for bearing fault detection and localization. In summary, this work is a first feasibility study of quasi-distributed strain sensing on the inner ring of a bearing. We demonstrate that strain can be measured on the inner ring, the resulting FBG signals are interpretable in terms of fault evolution, and they show potential for improved sensitivity and intrinsic fault localization. This contributes to more reliable and interpretable diagnostics for condition-based maintenance of rotating machinery. A comparison with other sensing technologies, such as, e.g., accelerometers, is outside the scope of this paper, but we consider it a crucial step for future work.

The rest of this paper is structured as follows. In Section 2 we describe our experimental setup for an accelerated lifetime test of a deep-groove ball bearing instrumented with FBG sensors in a fiber bonded on the inner ring. The analysis of the FBG signals during the complete accelerated lifetime test is presented in Section 3. We characterize the properties of the FBG signals in the time and frequency domains and, from our observations, we select different features and study their their capabilities for fault detection and localization over the course of the fault development. Finally, the main conclusions and future work topics are summarized in Section 4.

2. EXPERIMENTAL SETUP

2.1. Description of the bearing test setup

The bearing accelerated lifetime test in this study was performed in the Flanders Make's Smart Maintenance Living Lab (Ooijevaar et al., 2019). This lab is developed as an open test and development platform and aims to support the adoption of condition monitoring technologies in the industry. The setups are designed to perform accelerated lifetime testing of bearings and run bearings to their end-of-life. The accelerated lifetime test allows to create surface fatigue faults in bearings and monitor the fault evolution and accumulation during the (accelerated) life. The bearing model for this setup is the FAG 6205-C-TVH deep-groove ball bearing, manufactured by Schaeffler[1].

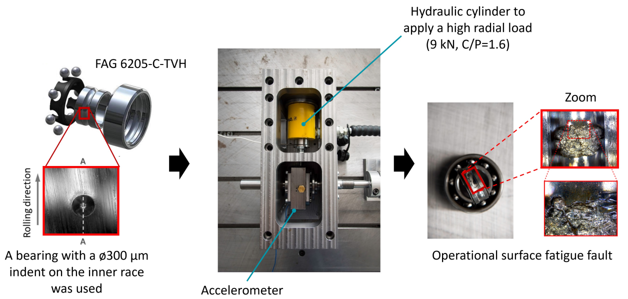

Figure 1. Illustration of the initial bearing state (left), the experimental test rig setup designed to perform accelerated life tests (middle), and an example of the final state, a surface fatigue fault at the inner race of the bearing (right). Note that 9 kN is the maximum possible load, while in this work the applied load is 7 kN, and the spall resulting from the experiment analyzed in this work is shown later in Figure 4.

One of these experimental accelerated lifetime test setups is shown in the middle image of Figure 1. The setup comprises of a single shaft with a test bearing, where the shaft is supported by a support bearing on each side. The test bearing is lubricated by an internal oil bath, using the Total Carter SH 220 oil[2]. The setup is driven by a motor at a rotation speed up to 3000 RPM. Each setup is equipped with an accelerometer, temperature sensor, load sensor and speed sensor. The radial accelerations are measured at a sampling frequency of 50 kHz by an accelerometer attached to the bearing housing. The rotational speed and radial load of each setup can be controlled, such that each setup can operate at stationary and non-stationary operating conditions. An industrial Beckhoff control platform is used to acquire and store the sensor signals and to control the speed and load of each setup.

2.2. FBG instrumentation on the test bearing and setup

An optical fiber with nineteen (19) FBG sensors of each 5 mm in length was bonded directly at the inner ring of the test bearing using the NOA81 UV-cured adhesive[3], following the same procedure described in (Goossens et al., 2025). The fiber with the FBGs covered the entire circumference of the

---

[1] `https://www.schaeffler.com/en/`

[2] `https://lubricants.totalenergies.com/`

[3] `https://norlandproducts.com/`

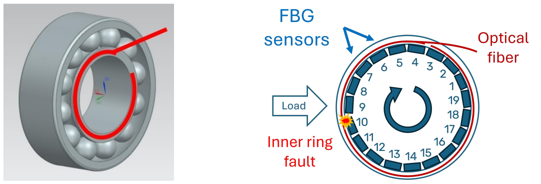

(a) Diagram of the optical fiber with integrated FBGs (red) bonded on the inner ring of the test bearing.

(b) Diagram of the location and numbering of the FBGs with respect to the inner ring fault.

Figure 2. Location of the optical fiber bonded on the test bearing's inner ring (left) and the FBG sensors integrated in the fiber (right).

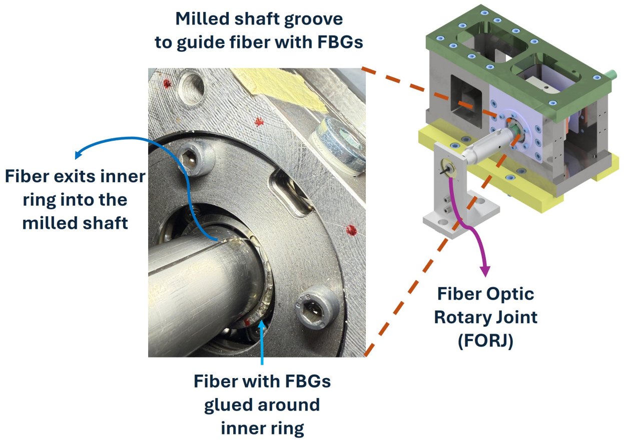

Figure 3. Illustration of the complete test setup, adapted for operation with an optical fiber bonded on the test bearing inner ring, and a close-up photograph of the adapted shaft with milled groove for fiber routing and protection.

inner ring, as depicted in Figure 2a. The numbering we use to refer to the FBG sensors is shown in Figure 2b, where it can be seen that the fault is located closest to FBG 10, and opposite to FBGs 17, 18 and 19. Note that the location of fault is known since it evolves from a small initial indentation in the inner race, as detailed in Section 2.3. The FBGs are stationary with respect to the fault, as they rotate together with the inner ring, and non-stationary with respect to the applied load. The fact that the fiber is bonded onto the rotating inner ring creates two main challenges to be able to successfully operate the setup, which are:

A: To preserve the integrity of the rotating fiber.

B: To connect the rotating fiber to a static fiber for data acquisition.

To address challenge A, we created a custom shaft with a milled axial groove that routes and protects the fiber during operation, and a cable drum that houses the excess fiber cable. Challenge B is addressed by a connection to a fiber optic rotary joint (FORJ), in particular the model BN549383C0100 from Spinner[4]. We designed a flexible mount for the FORJ stator, that compensates shaft deflection and run-out. The complete adapted test setup, with a close-up photograph of the milled axial groove at the shaft, is shown in Figure 3.

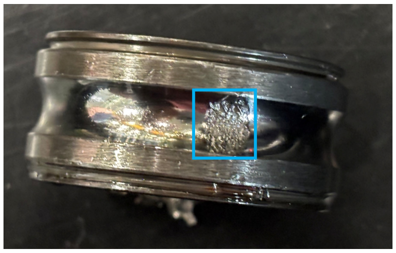

Figure 4. Resulting spall on the inner raceway at the end of the accelerated lifetime test.

2.3. Bearing accelerated lifetime test conditions

Two mechanisms are used to accelerate the bearing lifetime:

- A high radial load of a maximum of 9 kN (C/P = 1.6) is applied to the bearing outer ring with a hydraulic cylinder. In this work, the applied load was 7 kN.
- Before the start of the test a small initial indentation of approximately 300 µm was created in the bearing inner race using a Rockwell C hardness tester. This indentation is used as a local stress riser and represents a local plastic deformation caused by, for instance, a contamination particle.

The accelerated lifetime tests are stopped as soon as 25g peak-to-peak accelerations are reached, resulting in severe rolling contact surface fatigue at the inner race (Halme & Andersson, 2009). Examples of the start and end conditions of the inner race of a test bearing are shown in the left and right images of Figure 1.

In this work, we conducted an accelerated lifetime test on a single test bearing at 2000 RPM, with a radial load of 7000 N. The resulting spall on the inner race of the test bearing at the end of this experiment is shown in Figure 4.

2.4. FBG data acquisition

The data from the FBGs was acquired with an FBG-scan 704D interrogator by FBGS International[5], operating at a maximum sampling frequency of 4982 Hz, connected to the static side of the FORJ. This interrogator uses a broadband light source and spectrometer, covering a spectral range from 1520 to 1570 nm with a spectral hardware resolution of 10 pm. We recorded the wavelength of each FBG peak for 10 seconds every 5 minutes throughout the complete experiment. The reflection spectrum measured at the beginning of the experiment is shown in Figure 5. Each peak corresponds to the

---

[4] `https://www.spinner-group.com/`
[5] `https://fbgs.com/`

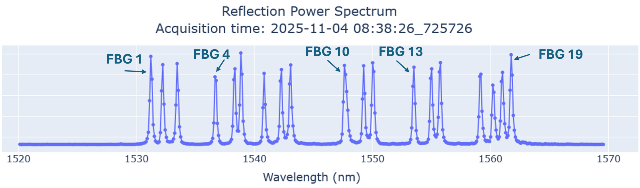

Figure 5. Reflection spectrum of the FBG sensors, indicating the 19 Bragg peaks, as measured at the beginning of the experiment.

reflection of an FBG, with FBG 1 relating to the leftmost peak and FBG 19 relating to the rightmost peak.

3. RESULTS AND DISCUSSION

3.1. Fault manifestation in the FBG signals

Each FBG sensor response corresponds to the central wavelength of its peak in the reflection spectrum, which varies over time according to the strain and temperature that it is subjected to due to the rotation of the setup and the radial load applied. The reflected peak wavelength λ_k of the k-th FBG sensor is related to the strain ε_k and the temperature change ΔT_k by (Hill & Meltz, 1997)

$$\frac{\Delta\lambda_k}{\lambda_{0,k}} = C_e \varepsilon_k + C_T \Delta T_k \,, \tag{1}$$

where $\lambda_{0,k}$ is the reference peak wavelength of the k-th FBG sensor, $\Delta\lambda_k = \lambda_k - \lambda_{0,k}$ is the wavelength shift, and C_e and C_T are fiber-dependent material constants. In our case, $C_e \approx 1.2$ pm /μstrain, and $C_T \approx 9 \cdot 10^{-6}$ per degree Celsius for a standard single-mode fiber at 1550 nm. Due to the linear relationship between strain and reflected wavelength in Eq. (1), in this paper we work directly the FBG reflected peak wavelength signal measured by the optical interrogator.

In Figure 6 we can observe that, when the bearing is in healthy[6] condition, the FBG signals look cleanly periodic and sinusoidal, both for the FBGs closest to the location of the initial indentation of 300 µm (Figure 6a) and those on the opposite side Figure (6b). This is due to the dominant contribution to the strain of the radial load, as the FBG sensors pass by the load zone at the frequency of the shaft rotation.

By contrast, on Figure 7 we can observe that, when the bearing fault has fully developed (see Figure 4), clear distortions appear in the FBG signals, both for the FBGs closest to the location of the initial indentation (Figure 6a) and those on the opposite side Figure (6b). However, these distortions are stronger in those FBGs closer to the fault, and appear in different moments in time. The distortions are consistent with the loss of load carrying capacity as a rolling element enters and exits the spall, as studied in (Medvedovsky et al., 2022) for outer race faults and in (Maljaars et al., 2025) for inner race faults using strain gauges installed on the outer ring.

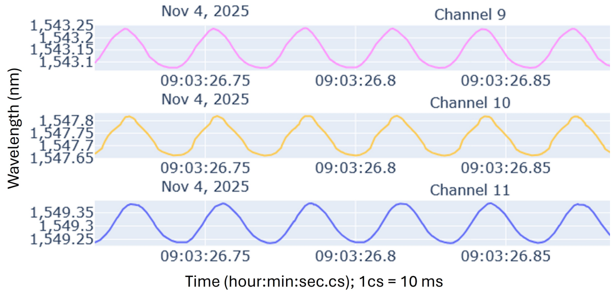

(a) FBG signals recorded by sensors 9, 10 and 11 (closest to the fault) with the test bearing in healthy condition.

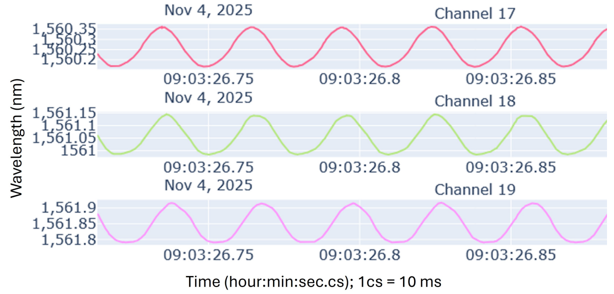

(b) FBG signals recorded by sensors 17, 18 and 19 (far from the fault) with the test bearing in healthy condition.

Figure 6. Sensor signals of six FBGs, close and far from the fault location, at the beginning of the experiment, when the fault has not yet developed in the test bearing.

In the frequency domain, it is interesting to look at the bearing fault frequencies, which correspond to the frequencies of the periodic impulses produced by a bearing fault. These fault frequencies depend on the fault location, bearing geometry, and rotational speed (Randall, 2011). Since we focus on an inner race fault in this study, the fault characteristic frequency is the ball pass frequency on the inner race (BPFI), given by

$$f_{\text{BPFI}} = \frac{n f_r}{2} \left\{ 1 + \frac{d}{D} \cos\phi \right\} , \tag{2}$$

where f_r is the shaft speed (frequency), n is the number of rolling elements, d is the diameter of the rolling elements, D is the pitch diameter , and ϕ is the contact angle. Other fault characteristic frequencies are the BPFO (ball pass frequency, outer race) and the BSF (ball spin frequency), corresponding respectively to outer race and rolling element faults.

By looking in Figure 8 at the magnitude spectrum of an FBG signal (in this case, FBG 10) acquired at moments of healthy and faulty conditions, we can confirm our observations from the time domain signals. The shaft harmonics are highly dominant when the bearing is healthy, as can be seen in Figure 8a, while the amplitude of the BPFI harmonics clearly increases

---

[6] We refer to healthy condition as the period of time when the fault as not yet developed enough to be detected, although due to the presence of the initial indentation a more precise adjective would be pseudo-healty. Note that the indentation is visible under a microscope.

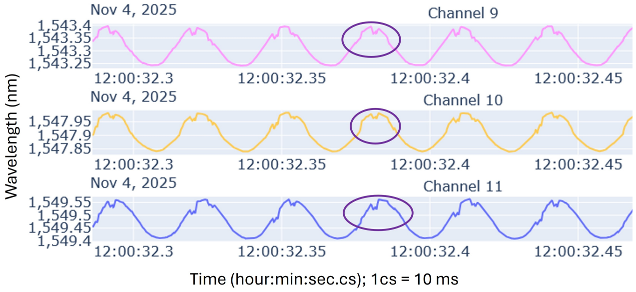

(a) FBG signals recorded by sensors 9, 10 and 11 (closest to the fault) with the test bearing in faulty condition.

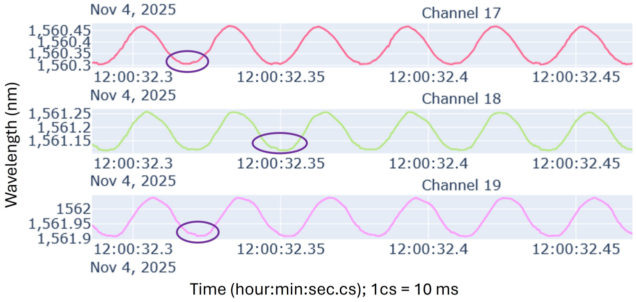

(b) FBG signals recorded by sensors 17, 18 and 19 (far from the fault location) with the test bearing in faulty condition.

Figure 7. Sensor signals of six FBGs, close and far from the fault location, at the end of the experiment, with a fully developed fault in the test bearing. Examples of distortions created by the fault are marked by circles.

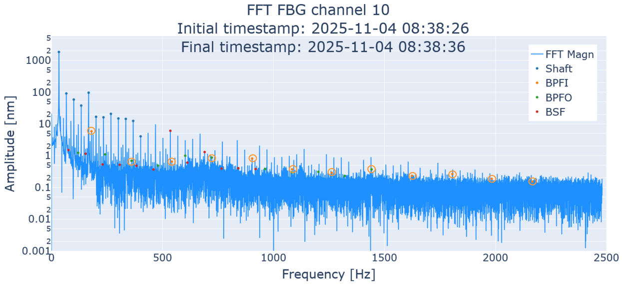

(a) FFT of the FBG 10 signal acquired with the test bearing in healthy condition, 10 minutes after the beginning of the experiment. Shaft harmonics are highly dominant.

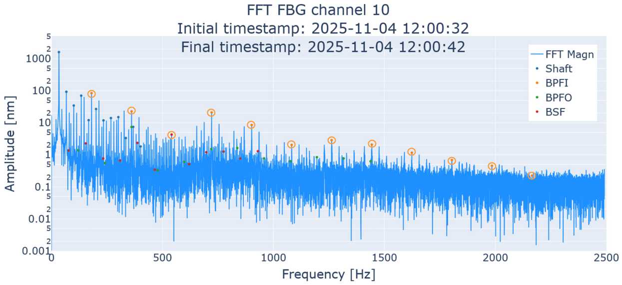

(b) FFT of the FBG 10 signal acquired with the test bearing in faulty condition, just before the end-of-life. BPFI harmonics can be clearly observed.

Figure 8. Magnitude of the FFT of sensor signals of FBG 10 during acquisitions on healthy and faulty conditions of the test bearing. The shaft, BPFI, BPFO, BSF frequencies and its harmonics are marked in different colours. The BPFI and its harmonics are additionally marked with circles.

when the fault has fully developed, as observed in Figure 8b.

3.2. Features for FBG-based fault detection

We turn our attention now to different features of the FBG signals that can be used to detect the presence and evolution of a bearing fault. Due to the presence of strong shaft harmonics in the FBG signals, a pre-processing step for all the features we consider is high-pass filtering the signals. In our case, we chose a Butterworth filter of order 12. To avoid removing the fundamental BPFI frequency of 180.93 Hz, the rejection band of our high-pass filter (HPF) only covers up to the 5th shaft harmonic of 166.66 Hz.

In the time domain, we consider two features to be computed from the FBG signal after pre-processing:

- root mean square (RMS) value,
- peak-to-peak (P2P) value.

The evolution of the RMS feature is depicted in Figure 9. During the initial stage, the RMS values of all FBG sensors are roughly clustered together, with the notable exception of FBG 10, whose RMS value is noticeably higher since the very beginning of the experiment. This is the FBG sensor placed closest to the small initial indentation of 300 µm, which was undetectable by vibration analysis of the accelerometer signal in our more than 70 previous experiments with this test setup. While this level of accuracy would need to be consistently demonstrated by further experiments, it is a promising observation. It can also be observed that there is a large increase in the RMS value of all sensors from 10:55 to 11:05, followed by a drop at 11:10. After the drop, from 11:20 onward, a distinction remains between the high RMS values of those sensors closer to the fault (FBGs 8 to 12) and the rest.

In the case of the P2P feature, its evolution for all FBG sensors is shown in Figure 10. The isolated spikes at 9:28 and 10:40 reach similar levels as the more sustained higher values later on, from 10:55 to 11:10. In the last stage, from 11:15, there is a decrease in feature value across all FBG sensors, The latter part could be caused by the smoothing of the spall, as more material is removed from its surface, since the RMS feature also presents a drop at 11:15 across all FBG sensors. This feature raises the question of whether the early spikes are reliable indicators of fault presence, and does not seem suited for consistent bearing fault detection.

In the frequency domain, we consider features based on the squared envelope spectrum (SES), a technique well established in vibration analysis for bearing diagnosis (Randall & Antoni, 2011). As was already observed from Figure 8a and 8b, the BPFI and its harmonics, even those of higher orders,

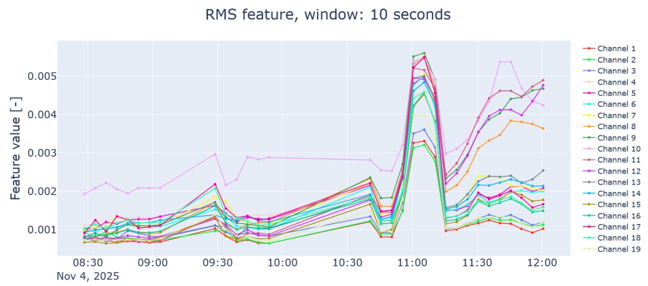

Figure 9. Evolution of the RMS feature of every FBG sensor over the complete accelerated lifetime test. Each point corresponds to the feature value calculated on 10 seconds of FBG data acquisition.

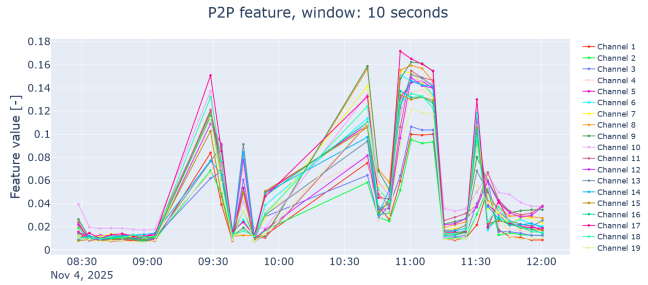

Figure 10. Evolution of the P2P feature of every FBG sensor over the complete accelerated lifetime test. Each point corresponds to the feature value calculated on 10 seconds of FBG data acquisition.

have a strong presence once the fault is developed, which can be distinguished even in the spectrum of the raw FBG signals. The SES is used in vibration analysis to enhance the useful diagnostic information, i.e., the fault frequencies' harmonics, since this information is obfuscated in the spectrum of the raw acceleration. Following these observations and as proposed in previous works (Medvedovsky et al., 2022; Goossens et al., 2025), we construct our BPFI feature as the sum of the SES value at the BPFI and its harmonics. Mathematically, it is expressed as

$$\xi_{\text{BPFI}} = \sum_{k=1}^{n_{\text{harm}}} Y(k f_{\text{BPFI}}), \tag{3}$$

where $Y(k f_{\text{BPFI}})$ denotes the peak magnitude of the SES at the k-th harmonic of the BPFI, and n_{harm} is the number of harmonics considered. Finding the peaks is done by searching the maximum SES magnitude around the theoretical fault frequency (Eq. 2) and its harmonics, within a pre-defined range tolerance. In this study, we chose $n_{\text{harm}} = 8$.

The evolution of this BPFI feature is depicted in Figure 11. A similar pattern to the RMS evolution can be observed, with a clearer distinction between low (healthy) and high (faulty) feature values. Both the BPFI and RMS features present spikes at 9:28 and 10:40, an increase across all FBG sensors from 10:55 to 11:10, and a drop at 11:15. The correlation between the BPFI and RMS features is expected, since the presence of impulses caused by the inner race fault contributes to both the magnitude of the BPFI harmonics in the SES and the RMS of the high-pass filtered FBG signals. Again, as with the P2P and RMS features, the isolated early spikes of 9:28 and 10:40 need further experimental confirmation of their reliability for early detection, but are promising.

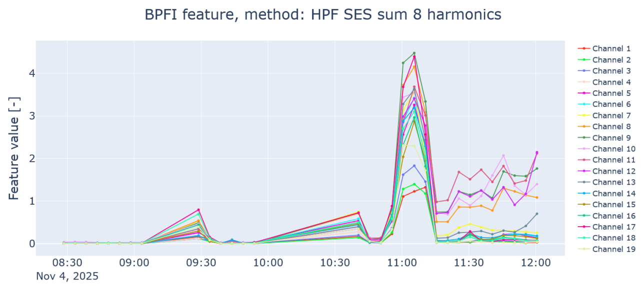

Figure 11. Evolution of the BPFI feature ξ_{BPFI} of every FBG sensor over the complete accelerated lifetime test, with $n_{\text{harm}} = 8$. Each point corresponds to ξ_{BPFI}, defined in (Eq. 3), calculated on 10 seconds of FBG data acquisition.

3.3. Fault localization

It could be observed already in Figures 6 and 7 that the disturbances created by the fault in the FBG signals are different depending on the relative position between each FBG sensor and the fault. As a natural consequence, the features of each FBG sensor behave differently according to this relative position, as was readily seen in Figures 9, 10 and 11. However, it is only the BPFI and RMS features that clearly reveal correlation between FBG and fault location. In these features, the FBG sensors 8 to 12, closest to the inner race fault, have higher values and a different pattern than those further away from it, i.e., FBGs 1 to 7 and 13 to 19. After the first large anomaly at 11:00, where feature values present a high increase for all FBG sensors, those of FBGs 8-12 present a growing trend at a higher value than 1-7 and 13-19, which stabilize around a significantly lower value. This is a valuable property of FBG sensing technology for diagnosis of rotating machinery, as fault localization can be performed simultaneously with fault detection using the same features.

4. CONCLUSION

In this work, we have presented a quasi-distributed sensing system of FBGs instrumented on the inner ring of a deep-groove ball bearing. The sensing system consists of nineteen (19) FBGs integrated on a single fiber, bonded directly to the inner ring. To study the bearing condition monitoring capabilities of this sensing system, we have performed an accelerated lifetime test on the bearing, running it to its end-of-life while a surface-initiated fatigue fault on the inner ring evolved from an initial micro-indentation to a fully developed spall. To the best of our knowledge, this is the first feasibility study of quasi-distributed strain sensing with FBGs instrumented on the inner ring of a bearing.

We have characterized the acquired FBG signals in the time and frequency domains, which served as basis to propose several features, both in the time and frequency domains, that allow to track the bearing fault evolution and monitor its condition. The behaviour of these features throughout the complete accelerated lifetime confirms their utility for bearing fault diagnosis. Additionally, fault localization can be obtained from certain features as a product of the same analysis performed for fault detection. This is a direct consequence of the possibility offered by FBG technology of integrating and multiplexing several FBG sensors in a single optical fiber. However, it is important to note that the instrumentation of the optical fiber with integrated FBGs on the inner ring presents a high degree of complexity, and requires careful installation to preserve the integrity of the fiber during operation. Other traditional sensing technologies, such as accelerometers, hold a lower degree of cost and complexity in their installation. Nevertheless, we highlight that quasi-distributed strain sensing on a rotating inner ring is not realistically achievable with conventional sensors (accelerometers or strain gauges) without significant complexity, so our proposed approach remains practical when targeting dense spatial sensing.

Future work includes confirming the potential for early fault detection, a better physical understanding of the strain signatures and distribution during bearing fault evolution, and an in-depth comparison with traditional bearing diagnosis technologies, such as vibration analysis of accelerometer signals.

The results of this work highlight the potential of FBG-based strain sensing to fundamentally enhance bearing diagnostics by combining high sensitivity, spatial resolution, and direct measurement of the underlying mechanical phenomena. Beyond demonstrating feasibility, this approach opens the path towards more physics-informed diagnostic models and improved prognostic capabilities, especially in environments where conventional sensing is limited by transfer path effects or electromagnetic interference. The ability to simultaneously detect and localize faults using a single multiplexed sensing network further supports scalable deployment in complex machinery, positioning FBG-based monitoring as a promising enabler for next-generation condition-based maintenance and digitalized industrial assets.

ACKNOWLEDGMENT

This research work was supported by Flanders Make, the strategic research centre for the manufacturing industry, and more precisely by the SAFOS SBO research project. The authors would like to thank this project for funding the research presented in this paper. The authors would also like to thank Yves Perremans and Jorre Goossens for their input and help during the setup design and initial data analysis, and Stefan Hendricx for his suggestions during the writing stage.

REFERENCES

Brusamarello, B., Cardozo da Silva, J. C., de Morais Sousa, K., & Guarneri, G. A. (2023). Bearing fault detection in three-phase induction motors using support vector machine and fiber Bragg grating. *IEEE Sensors Journal*, *23*(5), 4413-4421. doi: 10.1109/JSEN.2022.3167632

Eryilmaz, K., de la Hucha Arce, F., Zegers, J., & Ooijevaar, T. (2024, June). Noise-aware AI methods for robust acoustic monitoring of bearings in industrial machines. In *PHM Society European Conference* (Vol. 8). doi: 10.36001/phme.2024.v8i1.4112

Goossens, S., Berghmans, F., Muñoz, K., Jiménez, M., Karachalios, E., Saenz-Castillo, D., & Geernaert, T. (2021). A global assessment of barely visible impact damage for CFRP sub-components with FBG-based sensors. *Composite Structures*, *272*, 114025. doi: https://doi.org/10.1016/j.compstruct.2021.114025

Goossens, S., Mantas, P., Ojo, D., Axinte, O., Mauricio, A., Gryllias, K., & Berghmans, F. (2025, July 31). Repeatability assessment of FBG-based strain measurements for bearing fault diagnostics. *Journal of Physics: Photonics*, *7*(3), 1–13. doi: 10.1088/2515-7647/adec29

Halme, J., & Andersson, P. (2009). Rolling contact fatigue and wear fundamentals for rolling bearing diagnostics - state of the art. *Journal of Engineering Tribology*, *224*, 377–393.

Hill, K., & Meltz, G. (1997). Fiber Bragg grating technology fundamentals and overview. *Journal of Lightwave Technology*, *15*(8), 1263-1276. doi: 10.1109/50.618320

Jardine, A. K., Lin, D., & Banjevic, D. (2006). A review on machinery diagnostics and prognostics implementing condition-based maintenance. *Mechanical Systems and Signal Processing*, *20*(7), 1483-1510. doi: https://doi.org/10.1016/j.ymssp.2005.09.012

Maljaars, E., Ravesloot, J., Janssen, A., Mol, H., Murguia, C., & Fey, R. (2025). On the potential of rolling bearing strain signals for spall size estimation: Modeling and experiments. *Mechanical Systems and Signal Processing*, *240*, 113384. doi: https://doi.org/10.1016/j.ymssp.2025.113384

Medvedovsky, D., Ohana, R., Klein, R., Tur, M., & Bortman, J. (2022). Spall length estimation based on strain model and experimental fbg data. *Mechanical Systems and Signal Processing*, *171*, 108923. doi: https://doi.org/10.1016/j.ymssp.2022.108923

Ooijevaar, T., Pichler, K., Di, Y., Devos, S., Volckaert, B., Hoecke, S. V., & Hesch, C. (2019). Smart machine maintenance enabled by a condition monitoring living lab. *IFAC-PapersOnLine*, *52*(15), 376-381. (8th IFAC Symposium on Mechatronic Systems MECHATRONICS 2019)

Quatrini, E., Costantino, F., Di Gravio, G., & Patriarca, R. (2020). Condition-based maintenance—an extensive literature review. *Machines*, *8*(2). doi: 10.3390/machines8020031

Randall, R. B. (2011). *Vibration-based condition monitoring: Industrial, aerospace and automotive applications*. John Wiley & Sons, Ltd.

Randall, R. B., & Antoni, J. (2011). Rolling element bearing diagnostics—a tutorial. *Mechanical Systems and Signal Processing*, *25*(2), 485-520.

Zhang, H., Borghesani, P., Randall, R. B., & Peng, Z. (2022). A benchmark of measurement approaches to track the natural evolution of spall severity in rolling element bearings. *Mechanical Systems and Signal Processing*, *166*, 108466. doi: https://doi.org/10.1016/j.ymssp.2021.108466